Journal of Materials Chemistry A

Accepted Manuscript

ROYAL SOCIETY OF CHEMISTRY

www.rsc.org/materialsA

Hierarchical 3-Dimensional $CoMoO_4$ Nanoflakes on Macroporous Electrically conductive Network with Superior Electrochemical Performance

Mai Li[a,b], Shaohui Xu[a], Christopher Cherry[b,c], Yiping Zhu[a], Dajun Wu[a], Chi Zhang[a], Xiaolin Zhang[b], Rong Huang[a], Ruijuan Qi[a], Lianwei Wang[a,b*], Paul K. Chu[b*]

[a] Key Laboratory of Polar Materials and Devices, Ministry of Education, and Department of Electronic Engineering, East China Normal University, 500 Dongchuan Road, Shanghai 200241, P. R. China

[b] Department of Physics and Material Science, City University of Hong Kong, Tat Chee Avenue, Kowloon, Hong Kong, China

[c] Fischell Department of Bioengineering, University of Maryland, College Park, MD 20740, USA

***Corresponding authors:** LW Wang (Tel: +86-021-54345160; Fax: +86-021-54345119; Email: lwwang@ee.ecnu.edu.cn); PK Chu (E-mail: paul.chu@cityu.edu.hk)

Abstract

Nanoscale cobalt molybdate ($CoMoO_4$) particles are fabricated hydrothermally on the surface and sidewall of three-dimensional nickel-coated silicon microchannel plates (also called macroporous electrically conductive network, MECN) as the active electrode in a miniature energy storage device. The relationship among the reaction time, morphology, formation mechanism of the $CoMoO_4$ nanostructure, and electrochemical performance is studied. After an optimal hydrothermal synthesis time of 2.5 h, the $CoMoO_4$ electrode has a capacity of 32.40 mAh g^{-1} (492.48 μAh cm^{-2}) at constant current density of 1 A g^{-1} and retention ratio of 85.98% after 5,000 cycles. The large specific capacity and excellent rate capability can be attributed to the unique 3D ordered porous architecture which facilitates electron and ion transport, enlarges the liquid-solid interfacial area, and enhances the utilization efficiency of the active materials. Furthermore, the weight and size of the device are reduced. By using the $CoMoO_4$/MECN electrode as the positive electrode and Carbon/nickel foam (Carbon/NF) as the negative electrode, the faradaic electrode were packaged by CR2025 battery cell as the miniature hybrid device exhibits stable power characteristic (5,000 cycle times with 71.82% retention). After charging each hybrid device for 10 s, three devices in series can power two 5 mm diameter light-emitting diodes (LED) efficiently.

1. Introduction

To meet urgent needs for sustainable and renewable power sources in the modern electronics industry, much effort has been made to develop energy storage systems that allowing energy to be stored and used in demand [1-5]. Carbon-based electrochemical double layer capacitors (EDLCs) have been used in many applications such as power back-up, pacemakers, air bags, and electrical vehicles [1, 6] because of their high power density, long lifespan, and charge/discharge efficiency [2, 7-9]. While the unsatisfactory energy density (typically 5-10 Wh kg^{-1}) of EDLCs compared to lead acid batteries (30-40 Wh kg^{-1}), and lithium ion cells (160 Wh kg^{-1}) that limited their application in the industry world. The most widely known pseudocapacitors (PCs) are fabricated by the materials of MnO_2[10], RuO_2[11] as well as nitrides and carbides[12] that store energy using both ion adsorption and electron transfer processes, rather than simply relying on the accumulation of ions in the EDLCs[12, 13]. However, the dissolution and high resistance of MnO_2 [14, 15] in aqueous electrolyte, high price and toxic of RuO_2[16, 17] blocking them from large-scale usage. In this context, energy storage based on faradaic reaction has been the hot topic of interest in the recent years [18-20] which has the salient features including low maintenance, excellent efficiency, cycling stability and environmental friendly [21]. Hybrid device fabricated by faradaic electrode bridge the gap between EDLCs and PCs. A range of candidates can be employed as electrodes for hybrid devices [21]. Now, the researchers fuscous on those faradaic electrodes working through chemical reaction as one of solutions to enhance the energy density without much attenuation of the power density that make up the deficiencies of electrochemical capacitors (ECs, also known as "supercapacitors").

Recently, binary metal oxides and mixed metal oxides have been reported to deliver better performance than single component oxides act as the active materials of faraday electrode due to the mixed oxidation states and high electrical conductivity. Materials such as $ZnCo_2O_4$ [22]. Zn_2SnO_4 [23], $NiCo_2O_4$ [24], $NiMoO_4$, [25] and $CoMoO_4$ [9, 26] are

promising materials for hybrid device[27]. $CoMoO_4$ is particularly attractive among those materials because it is economical, non-toxic and enhanced electrochemical properties. However, there have only been few reports on the faradaic behavior of $CoMoO_4$ so far and the detailed electrochemical behavior of $CoMoO_4$ nanosturctures is not yet well established. There are mainly two techniques to prepare $CoMoO_4$ electrode materials, namely low-temperature chemical precipitation[28, 29] and hydrothermal synthesis [6, 25, 27, 30]. Low-temperature chemical precipitation has been adopted to deposit $CoMoO_4$ nanorods [28] and particles [29] as the active materials, but the method tends to be complicated and time consuming and the repeatability is relatively poor. In comparison, hydrothermal synthesis has several advantages. Firstly, instead of producing the active materials in a complex environment, the materials can be deposited directly on a substrate and hence, the microstructure of the active materials can be preserved. Secondly, the active materials can be deposited directly without the need of adding a polymer binder and conduction agent, so the conductivity and purity of the active materials will not be affected by additives. Thirdly, when the reaction is carried out at a high temperature and pressure, the solution can easily penetrate the nanoscale electrode substrate so that the hierarchical $CoMoO_4$ nano-sturcture grows uniformly on both the surface and sidewall of the macroporous electrically conductive network (MECN) which was fabricated by ordered porous silicon microchannel plates (Si-MCP) with a depth of 300μm [Fig.2(a)] [17].

To improve the faradaic behavior, it is crucial to enhance the kinetics of ion and electron transport inside the electrodes and at the electrode/electrolyte interface. Macroporous three-dimensional (3D) structures acting as conductive networks enable access of ions and electrons to the active surface and produce a better electrochemical response on the electrodes. Obviously, the structure and morphology of the electrode materials are important due to limitations imposed by ion and electron transport. Herein, we report a hydrothermal strategy to prepare ordered hierarchical $CoMoO_4$ films as high performance faradaic electrode active material. Macroporous electrically conductive

network (MECN) with a large aspect ratio is combined with transition metal hydroxide to produce the novel hybrid device. The inner wall of the MECN provides all the space needed for the nickel current collector layer and $CoMoO_4$ active materials, so the footprint of the electrode can be reduced while maintaining the advantage of a large surface area for the active materials due to the nanocrystals on the inner wall of the macroporous. Fig. 1 illustrates the large specific surface area concept and unit structure of the miniature electrode to clearly demonstrate the advantages. The thin $CoMoO_4$ nano-flake films are deposited on the nickel-coated MECN for different time of 0.5, 1.2, 1.8, and 2.5 h. The electrochemical properties and effects of the solvents on the morphology of the $CoMoO_4$ films are determined from an area of 0.5 cm^2.

2 Experimental details

2.1 Chemicals

The chemical reagents, including sodium chloride {$NiCl_2•6H_2O$}, sodium hypophosphite monohydrate {$NaH_2PO_2•H_2O$}, ammonium chloride {NH_4Cl}, chloride hexahydrate {$CoCl_2•6H_2O$}, and ammonium molybdate tetrahydrate {$(NH_4)_6Mo_7O_{24}•4H_2O$} were AnalaR (AR) grade and used as received without further purification. The aqueous solutions were prepared with 18 MU de-ionized water and all the experiments were carried out at room temperature.

2.2 Fabrication of the low-resistance macroporous electrically conductive network

The nickel layer was deposited on both the outer surface and inner side wall of the silicon micro channels (Si-MCP) as illustrated in Fig. 2(b)-(d). The macroporous electrically conductive network was prepared according to Ref.31, based on Si-MCP [32]. In order to improve the surface area and conductivity of the MECN, porous nano-Ni shown in Fig. 2(b)-(d) was created by the electrochemical nickel-plated method. Electrodeposition of the porous nano-Ni film was performed in a standard two-electrode

glass cell at 23±1 °C in an electrolyte consisting of 2 M NH_4Cl and 0.1 M $NiCl_2$ at a pH value of 3.5 with the clean MECN as the working electrode and Pt foil as the counter electrode. The distance between the two electrodes was 1 cm and electrodeposition was carried out at a constant current of 0.25 A cm^{-2} for 90 s.

2.3 Synthesis of the hierarchical 3-Dimensional $CoMoO_4$ nanoflakes

$CoMoO_4$ was prepared hydrothermally. The macroporous electrically conductive network (MECN) were cut into small thin foils with an area of 0.8×0.9 cm, put into a buffer solution of Triton X-100 for at least 2 minutes to increase the hydrophilicity, and then placed standing against the wall of a Teflon-lined autoclave. The reaction solution was obtained by mixing 0.4 mmol of $CoCl_2•6H_2O$ and 0.4 mmol of $(NH_4)_6Mo_7O_{24}•4H_2O$ in 100 mL of distilled water under magnetic stirring and then transferred into a Teflon-lined stainless steel autoclave liner. The reaction proceeded for 0.5 h (Sample-0.5h), 1.2 h (Sample-1.2h), 1.8 h (Sample-1.8h) or 2.5 h (Sample-2.5h) resulting in the formation of a violet precipitate containing $CoMoO_4•H_2O$ on the surface of MECN. The purple product was taken out and rinsed ultrasonically in de-ionized water and ethanol. The process was repeated several times until the product was free of impurities. Finally, the MECN with the as-grown hydrate precursors were dried at 80°C for 2 h and then annealed at 300°C for 2 h in pure argon to obtain the $CoMoO_4$/MECN. In order to study the performance of the device with a planar structure, the $CoMoO_4$ was prepared on a Ni-covered silicon wafer for comparison. The fabrication steps and size of $CoMoO_4$/Ni/Si (Sample-2D) are the same as the $CoMoO_4$/MECN reacted for 2.5 h.

2.4 Characterization

The morphology and microstructure of the MECN and $CoMoO_4$ thin films were examined by field-emission scanning electron microscopy (FE-SEM, JEOL JSM-7001F, Japan) and the crystal structure was determined by X-ray diffraction (XRD, Rigaku, RINT2000, Japan). The Raman spectra was recorded from 200 to 1200 cm^{-1} on an

Olympus BX41 Raman Microprobe using a 524.5 nm argon ion laser. The electrochemical measurements were performed on a three-electrode electrochemical working station (Shanghai Chenhua CHI660D) with the saturated calomel electrode and platinum gauze electrode serving as the reference electrode and counter electrode, respectively. The measurements were conducted at room temperature in a 2 M KOH aqueous electrolyte. In order to determine the electrochemical properties and specific capacity of the electrode samples, CV scans were acquired from 0 to 0.6 V (vs. SCE) from each sample at different scanning rates. Charge-discharge cycle tests were conducted in the potential range between 0 and 0.45 V at different constant current densities. With regard to the hybrid device, CV scans were acquired from -0.1 to 0.8 V at different scanning rates and the charge-discharge cycle tests were conducted in the potential range between 0 and 0.8 V at different constant current densities.

3. Results and discussion

3.1 Characterization of the thin $CoMoO_4$ nanoflakes

The morphology of the $CoMoO_4$ nanoflakes on MECN are shown in Figs. 3 (a)-(c) depicting the SEM images of $CoMoO_4$ viewed from the top. The $CoMoO_4$ nanoflakes stand on the Ni support layer and are interconnected with each other forming an ordered array with an open network. As a result, most of the nanoflakes surface is readily accessible by the electrolyte when used as the faradaic electrode. According to the higher magnification SEM images in Figs. 3(b) and (c), the average thickness of a single nanoflake is about 100 nm. Figs. 3(d)-(f) exhibit the SEM images of the $CoMoO_4$ nano-columns from the inner surface on the side wall of the MECN at different magnifications. The $CoMoO_4$ nano-columns with an uneven surface have a typical length of 1 μm and width of about 200 nm. The nickel particles can provide a vast quantity of sites for fabricating the $CoMoO_4$ nano-columns thereby resulting in a high mass loading of the $CoMoO_4$ nano-columns. The nanoflakes on the surface and nano-columns on the side wall of the MECN work together to improve the performance of the

electrode by increasing the total contact area of the materials with the KOH electrolyte and providing more electroactive sites for faradaic reactions leading to high area capacity. Compared with the active materials prepared on the MECN, the nanostructured $CoMoO_4$ on nickel covering the Si wafer shown as Fig.(g) and (h), that has a different morphology. The tile-like structure on the Ni/Si replaces the crystal-shape nano-flake on the MECN. The altered nanostructure of $CoMoO_4$ and substrate undermines the performance of the electrochemical electrode. The $CoMoO_4$/MECN sample with a hydrothermal time of 3.2 h (Sample-3.2h) was synthesized with other conditions unchanging. As shown in the SEM images of Fig.S1 (a) and (b), the MECN is almost entirely blocked by the compact $CoMoO_4$ that may improve the resistance of the MECN electrode that weakened the overall electrochemical performance of the electrode. The long time deposition of $CoMoO_4$ structure formation of a unitary structure on the surface of MECN is easy to drop during the long time faradaic reactions.

To determine the phase structure of the products, X-ray diffraction (XRD) is conducted. The backbone materials MECN (Ni: JCPDS card No. 01-089-7128) are identified by the XRD pattern in Fig. 4(a) (top line). The hierarchical $CoMoO_4$ heterostructure ($CoMoO_4$: JCPDS card No. 00-021-0868) is identified in Fig. 4(a) (bottom line) and Fig. 4(b) displays the Raman spectra of the $CoMoO_4$ particles with peaks at 335, 364, 817, 880, and 936 cm^{-1}. According to Pasquan et al.[29, 33], pure $CoMoO_4$ shows a strong band at 940 cm^{-1} and weaker bands at 700, 813, and 880 cm^{-1}. The Raman bands at 880 and 940 cm^{-1} and broad band at 350 cm^{-1} can be assigned to Mo-O-Co stretching vibrations in cobalt molybdate [34].

Transmission electron microscopy (TEM) is carried out to further investigate the structure of the as-synthesized $CoMoO_4$. Figs. 4(c) and (d) depict the typical TEM images of $CoMoO_4$ after ultrasonic treatment in ethanol. The selected-area electron diffraction (SAED) patterns of the representative nanoflakes are shown in the inset of Fig. 4(c). The HR-TEM image in Fig. 4(d) reveals lattice fringes of 0.67 nm,

corresponding to the (001) plane of β-$CoMoO_4$ [18].

3.1 Crystal growth mechanism and morphology of the thin $CoMoO_4$ nanoflakes

The reaction can be described as follows [35]:

$$(NH_4)_6Mo_7O_{24}\bullet 4H_2O + 7CoCl_2\bullet 6H_2O \rightarrow 7CoMoO_4 + 6NH_3 + 14HCl + 42H_2O. \quad (1)$$

Fig. 5(a) shows the nanostructured $CoMoO_4$ in the early nucleation stage as manifested by small nano-dots and nano-flakes on the surface of the MECN. Unlike the film formation process, crystal growth roughens the surface of the substrate further increasing the specific surface area of the electrode. Fig. 5(b) shows the nanoflake $CoMoO_4$ growth on the nanometer scale and the network-like structure including interconnected nanoflakes exhibiting anisotropic morphological characteristics. After formation of the nano-rods and discrete nano-dots and nano-flakes as shown in Fig. 5(a), the joints may also be the nucleation centers for the growth of the $CoMoO_4$ nanoflakes. Compared to the nanostructured $CoMoO_4$ shown in Fig. 5(b), a large amount of $CoMoO_4$ can be found from Fig. 5(c) showing a narrow mesoporous distribution at around 500 nm. In the crystallization process, the system is in a dynamic state of change which determines the crystal morphology. The balance between the surface free energy and volume free energy determines the size of the crystal. Fig. 5(d) shows that the $CoMoO_4$ nanoflakes on the surface play an important role in the electrochemical accessibility of OH^- to the active materials and fast diffusion rate in the redox phase. Hence, for the samples deposited for different time, the temperature is optimized and the testing conditions of each sample are unchanged.

3.2 Electrochemical characterization

By altering the hydrothermal synthesis time while keeping the other parameters the same, the surface coverage, amount of coated $CoMoO_4$, and electrical characteristics of the sample are evaluated. Cyclic voltammetry (CV) and chronopotentiometry are

conducted to determine the specific capacity and electrochemical properties of the $CoMoO_4$ electrodes. Fig. 6(a) discloses that the capacity of the $CoMoO_4$ fabricated on the nickel covered silicon is negligible. The $CoMoO_4$/MECN shows considerably larger capacity because of the large enclosed area in the CV curve (10 mV s^{-1}) and longer discharging time [Fig. 6(b), 4 mA cm^{-2} charging-discharging current] as the electrodeposition time is increased. However, as shown in Fig. 6(a), Sample-2.5h has a similar enclosed area as Sample-1.8h but much larger area than Sample-0.5h and Sample-1.2h because Sample-2.5h has more abundant nanostructures. From the Fig.S2 of the supplementary information, the Sample-3.2h shows a different kind of CV curves compare with the Sample-2.5h which has a relatively small coverage area and high contact resistance. As expected, Sample-2.5h shows a longer discharging time than the other electrodes but less symmetrical charge-discharge curves indicating large charge current leakage. The other charging and discharging curves are more symmetrical indicating fully reversible electrochemistry. This is due to the presence of more active substances on Sample-2.5h narrowing the MECN pores consequently reducing the contact between the electrolyte and active substance. As shown in Fig. S2, Sample-3.2h has a 10% larger capacity compared with Sample-2.5h. The feature of charge-discharge voltage plateau from Sample-3.2h is much different from that of the approximately triangular curve of Sample-2.5h that may indicate that Sample-2.5 is closer to ideal pseudocapacitance[13, 36]. Sample-3.2h has a large IR drop and low coulomb efficiency that may reduce the overall performance of the electrode (Fig. S3).

The typical CV curves obtained at various scanning rates from Sample-2.5h are displayed in Fig. 6(c). As the scanning rate increased from 8 to 120 mV s^{-1}, the peak current is increased step by step. The oxidation and reduction peaks are apparent and peak shape is similar. However, the peak potential shifts to the anodic and cathodic directions, respectively, because of more substantial polarization at larger scanning rates. As the scanning rate is increased, the peak currents are proportional to the square root of the scanning rates, implying that the electrodes have good electrochemical performance

(Fig. S4). In the reverse scanning direction, the current is almost instantaneous. Moreover, in the CV curve, there is a small angle along the horizontal axis indicating that the electrodes have smaller impedance. The faradaic reactions corresponding to the redox peaks are shown in the following [37]:

$$3[Co(OH)_3]^- \Leftrightarrow Co_3O_4 + 4H_2O + OH^- + 2e^- \quad (2)$$

$$Co_3O_4 + H_2O + OH^- \Leftrightarrow 3CoOOH + H_2O + e^- \quad \text{and} \quad (3)$$

$$CoOOH + OH^- \Leftrightarrow CoO_2 + H_2O + e^-. \quad (4)$$

The two pairs of visible redox peaks in the CV curves confirm reactions (2), (3), and (4), suggesting that instead of a pure electrical double-layer capacitance, the measured faradaic electrode is dominated by a redox mechanism. It should be emphasized that the anodic peak potential, CV change, and cathodic peak potential shift in the anodic and cathodic directions with increasing sweeping rate that decrease the capacity.

To evaluate the application potential of the 3D MECN comprising the nanosturctured electrode (Sample-2.5h), the charging-discharging characteristics are evaluated at various current densities from 0.125 to 2 A g^{-1}. According to the chronopotentiometric results in Fig. 6(d) and total $CoMoO_4$ mass loading of 7.6 mg, the specific capacity (area capacity) values of Sample-2.5h are calculated to be 41.69, 39.88, 35.69, 32.40 and 26.40 mAh g^{-1} (633.7, 606.2, 542.5, 492.5 and 401.3 μAh cm^{-2}) for discharging current densities of 0.15, 0.3, 0.5, 1 and 2 A g^{-1}, respectively [24, 25]. The results obtained from Sample-2.5h are much larger than those from the $CoMoO_4$/MWCNTs electrode (21.33 mAh g^{-1} at a discharge current density of 1A g^{-1}) described by Xu et al. [35], pure $CoMoO_4$ nanostructure (20.68 mAh g^{-1} at a discharge current of 1A g^{-1}) reported by N. Padmanathan et al.[16], micro Li-ion capacitor with activated carbon/graphite configuration for energy storage (180 μAh cm^{-2} at a discharge current of 0.5 mA cm^{-2}) researched by Siwei Li et al.[38] and comparable to those obtained from the hierarchical $MnMoO_4$/$CoMoO_4$ heterostructured nanowires (51.99 mAh g^{-1} at a discharge current of 1A g^{-1}) prepared by Ma et al [6]. The units are all unified scientifically with respect of the original units used in the article given by the authors.

Long-time performance tests are carried out to evaluate the stability of the samples and the results are shown in Fig. 7(a). The Sample-2D has a 92.45% sharply capacity drop from 42.50 μAh cm^{-2} to 2.875 μAh cm^{-2} in the 2500 cycles that may due to the smooth structure of nickel deposition on the 2D silicon wafer against the firmly fixed of $CoMoO_4$ during its faraday reaction. The capacity of Sample-0.5h, and Sample-1.2h are unstable in the 5,000 cycle test and a capacity retention of less than 50% is achieved after 5,000 cycles at a current density of 20 mA cm^{-2}. The quick capacity drop observed from the three samples may arise from nanoparticles with more active sites on the sample surface detached from the substrate thus causing larger consumption in the electrochemical reaction. While the capacity of Sample-1.8h shows 78.49% retention because of the largest amount of active materials in the MECN pores and close integration with MECN, Sample-2.5h shows 85.98% capacity retention which is the best. The capacity reduction may originate from slow oxidation of $CoMoO_4$ because Co^{3+} is more stable than Co^{2+} under alkaline conditions and on account of reduced amount of active materials on MECN. The loose nano-flakes on the $CoMoO_4$/MECN yield a larger double layer capacitance which may originate from the porous structure of the sample that can fully contact the solution, but as shown by Fig. 7(a), after 5,000 cycles, some flakes are destroyed [39].

EIS is performed on the $CoMoO_4$ electrodes of Sample-2.5h with AC perturbation of 5 mV from 0.01 Hz to 100,000 Hz. Fig. 6(b) shows the EIS data obtained from the $CoMoO_4$/MECN before and after the long-term performance test. The equivalent circuit and results in the inset are fitted to the impedance spectra [40]. The electrode internal resistance R_1 is around 1.8 Ω indicating a highly conductive nature. The faradaic charge transfer resistance (R_2) corresponds to the semicircle in the high frequency range associated with the surface properties of the electrode. In the equivalent circuit, we introduce the constant phase element (CPE) component [40]. CPE_1 and CPE_2 represent the double-layer and faradaic capacity that vary with frequencies, respectively. This modification from a pure capacitance behavior can be explained by the distribution

effects [41] and porosity [42] of our samples. On account of the influence of the 3D structure of the MECN on mass transport, CPE_3 represents the Warburg impedance [43].

The table in Fig. 6(b) shows that $CoMoO_4$/MECN has an R_2 value of 0.225 Ω. After 5,000 cycles, the value is 0.285 which is consistent with the double-layer capacitance $CPE_{1\text{-}n}$ of $CoMoO_4$/MECN (0.784) and after 5,000 cycles (0.856). The loose nanoflakes on the $CoMoO_4$/MECN yield a larger double layer capacitance which may originate from the porous structure of the sample that can fully contact the solution but after 5,000 cycles, some flakes may be destroyed [40]. The capacity is originated from electrochemical reaction and so the parameters R_3 and $CPE_{2\text{-}n}$ are the key performance indicators. The R_3 values of electrodes before and after 5,000 cycles are 4.566 and 8.746, respectively, suggesting that the sample has more active materials and can react readily with the electrolyte. Comparison of the index of $CPE_{2\text{-}n}$ shows that the newly made sample has a $CPE_{2\text{-}n}$ of 0.787 that is larger than that after 5,000 cycles of 0.747 [44]. Furthermore, the slope of the impedance plots ($CPE_{3\text{-}n}$) is 0.982 compared to 0.822 of the old sample at low frequencies. This indicates that the special complex microstructure with flakes and particles in the new sample enables faster ion diffusion through the channels of the MECN.

3.3 Electrochemical properties of the $CoMoO_4$ hybrid device

To further evaluate the commercial potential of the $CoMoO_4$/MECN electrode, a hybrid device composed of the $CoMoO_4$/MECN electrode as the anode and activated CNTs on nickel foam as the cathode in a quasi-solid electrolyte together with one piece of cellulose paper as the separator is prepared. They are packaged by a CR2025 standard battery cell that composition of the hybrid device [45]. As shown in Fig. 8(a), three devices are assembled in series and after charging each device for 10 s, which can power both 5 mm diameter yellow (1.8 V, 20 mA) and blue (3.4 V, 20 mA) round light-emitting diodes (LED) efficiently. The oxidation and reduction peaks can be observed from Fig. 8(a) and the peak current become larger as the scanning rate is increased from

10 to 160 mV s^{-1}. However, there is no obvious distortion in the CV curve even at a scanning rate of 160 mV s^{-1}, corroborating the fast charging-discharging properties of the device [46]. In order to further evaluate the performance of the cell, the CP test is performed at various current densities. As illustrated in Fig. 8(b), the shape of the CP curves at different current densities resembles a triangle and the discharging curves show a good discharge platform at around 0.6 V, suggesting a rapid I-V response and good electrochemical reversibility. Fig. 8(c) reveals the outstanding cycling life of the device up to 5,000 times at large charging-discharging current of 2 mA cm^{-2}, which has rarely been demonstrated from quasi-solid electrolyte based hybrid device. Because of the activation process, the cycling capability of the hybrid device is completely activated and dramatically improved at the first 480 cycles (100% capacity at the 480th cycle) [47, 48]. When it approaches 2,700 cycles at the large current, the capacity exhibits a 20% loss and after this significant attenuation, the capacity approaches stabilizes in the following 2,300 cycles.

In order to explain the significant attenuation of the hybrid device with cycles, EIS is performed. The Nyquist plots after the activation process and 5000th charge-discharge cycles are exhibited in Fig. 8(d) and the corresponding equivalent circuits and fitting parameters are presented in Fig. 8(d). The open circuit voltage (OCV) of the MECN anodes after the activation process and 5000th charge-discharge cycles is also shown in Fig. 8(d). The impedance measurements after the activation process are shown in Fig. 8(d) can be analyzed as follows. The spectra at frequencies above 2 kHz are dominated by connections including external cell connections, electronic conduction between the substrate and active materials, and ionic conduction through the electrolyte. In our circuit model, the resistor R_0 is used to simulate the pure resistive behavior. The semicircle between 2 kHz and 50 Hz is related to the solid electrolyte interface (SEI) layer, which can be simulated by a resistor R_1 in parallel with a constant phase-angle element (CPE) named C_1. The impedance between 50 Hz and 0.01 Hz can be attributed to the charge transfer and diffusion of OH^- ions from the reaction interface to the bulk of

the pours of MECN. Another CPE named C_2 in parallel with resistor R_2 is employed to simulate the charge transfer behavior. Finally, a Warburg impedance W_0 is used to simulate the behavior of diffusion of OH^- ions.

According to the table in Fig. 8(d), the contact resistance R_0 of the sample after 5,000 cycles is 27.15 which is much larger than that of the initial sample [3.629] because the long cycling test damages the conduction between the Si substrate and Ni particles. In addition, resistance R_1 associated with the SEI layer of the sample after 5,000 cycles is 14.86 which is much larger than that of the initial sample [2.918] perhaps due to damage of the porous architecture of the electrode. R_2 for the circular arc diameter of the sample after the test is larger than that of the initial sample. It can be attributed to the gradual damage of the Ni coating and structure of $CoMoO_4$ nano-flakes with time and increasing difficulty for OH^- diffusion from the reaction interface to the bulk of the MECN.

4. Conclusion

$CoMoO_4$ nano-flakes produced uniformly on 3D MECN hydrothermally enable synergistic contributions from both the active materials and substrate giving rise to better electrochemical performance. The $CoMoO_4$/MECN have a large specific capacity of 35.69 mAh g^{-1} (492.48 μAh cm^{-2}) at 1 A g^{-1} and the retention ratio is 85.98% after 5,000 cycles. The hybrid device is composed of the $CoMoO_4$/MECN have high specific energy densities at various power densities as well as superior cycling stability. Our results suggest that thin $CoMoO_4$ is promising materials that bridge the gap between electrochemical double layer capacitors and pseudocapacitors that spurring a new and affordable approach to integrate Si processing into energy storage devices.

Acknowledgments

This work was jointly supported by Shanghai Pujiang Program (No. 14PJ1403600), Shanghai Fundamental Key Project (No. 11JC1403700), National Natural Science Foundation of China (No. 61176108), PCSIRT, Research Innovation Foundation of ECNU (No. 78210245), Guangdong-Hong Kong Technology Cooperation Funding Scheme (TCFS) GHP/015/12SZ, and City University of Hong Kong Applied Research Grant (ARG) No. 9667085.

References

1. J. R. Miller and P. Simon, *Science Magazine*, 2008, 321, 651-652.
2. P. Simon and Y. Gogotsi, *Nature materials*, 2008, 7, 845-854.
3. Y. Wang and G. Cao, *Advanced Materials*, 2008, 20, 2251-2269.
4. B. Tian, T. J. Kempa and C. M. Lieber, *Chemical Society Reviews*, 2009, 38, 16-24.
5. B. Tian, X. Zheng, T. J. Kempa, Y. Fang, N. Yu, G. Yu, J. Huang and C. M. Lieber, *Nature*, 2007, 449, 885-889.
6. L.-Q. Mai, F. Yang, Y.-L. Zhao, X. Xu, L. Xu and Y.-Z. Luo, *Nature communications*, 2011, 2, 381.
7. D. Zhu, Y. Wang, G. Yuan and H. Xia, *Chemical Communications*, 2014.
8. C. Zhou, Y. Zhang, Y. Li and J. Liu, *Nano letters*, 2013, 13, 2078-2085.
9. X. Yu, B. Lu and Z. Xu, *Advanced Materials*, 2014, 26, 1044-1051.
10. J. Yan, E. Khoo, A. Sumboja and P. S. Lee, *Acs Nano*, 2010, 4, 4247-4255.
11. C.-C. Hu, K.-H. Chang, M.-C. Lin and Y.-T. Wu, *Nano Letters*, 2006, 6, 2690-2695.
12. P. Simon, Y. Gogotsi and B. Dunn, *Science Magazine*, 2014, 343, pp. 1210-1211.
13. T. Brousse, D. Bélanger and J. W. Long, *Journal of The Electrochemical Society*, 2015, 162, A5185-A5189.
14. T. Wang, Z. Peng, Y. Wang, J. Tang and G. Zheng, *Scientific reports*, 2013, 3.
15. Y. Huang, Y. Huang, W. Meng, M. Zhu, H. Xue, C.-S. Lee and C. Zhi, *ACS applied materials & interfaces*, 2015.
16. N. Padmanathan, K. M. Razeeb and S. Selladurai, *Ionics*, 2014, 20, 1323-1334.
17. M. Li, S. Xu, T. Liu, F. Wang, P. Yang, L. Wang and P. K. Chu, *Journal of Materials Chemistry A*, 2013, 1, 532-540.
18. Z. Wu, X.-L. Huang, Z.-L. Wang, J.-J. Xu, H.-G. Wang and X.-B. Zhang, *Scientific reports*, 2014, 4.
19. L. Li, Z. Wu, S. Yuan and X.-B. Zhang, *Energy & Environmental Science*, 2014, 7, 2101-2122.
20. X.-l. Huang, J. Chai, T. Jiang, Y.-J. Wei, G. Chen, W.-q. Liu, D. Han, L. Niu, L. Wang and X.-b. Zhang, *Journal of Materials Chemistry*, 2012, 22, 3404-3410.
21. R. Ramkumar and M. Minakshi, *Dalton Transactions*, 2015, 44, 6158-6168.
22. K. Karthikeyan, D. Kalpana and N. Renganathan, *Ionics*, 2009, 15, 107-110.
23. L. Bao, J. Zang and X. Li, *Nano letters*, 2011, 11, 1215-1220.
24. L. Shen, Q. Che, H. Li and X. Zhang, *Advanced Functional Materials*, 2014, 24, 2630-2637.
25. D. Cai, B. Liu, D. Wang, Y. Liu, L. Wang, H. Li, Y. Wang, C. Wang, Q. Li and T. Wang, *Electrochimica Acta*, 2014, 115, 358-363.
26. D. Cai, B. Liu, D. Wang, L. Wang, Y. Liu, H. Li, Y. Wang, Q. Li and T. Wang, *Journal of Materials Chemistry A*, 2014, 2, 4954-4960.
27. X. Yu, B. Lu and Z. Xu, *Advanced Materials*, 2014, 26, 1044-1051.
28. M.-C. Liu, L.-B. Kong, C. Lu, X.-M. Li, Y.-C. Luo and L. Kang, *Materials Letters*, 2013, 94, 197-200.
29. C. T. Cherian, M. Reddy, S. C. Haur and B. Chowdari, *ACS applied materials & interfaces*, 2013, 5, 918-923.

30. D. Guo, H. Zhang, X. Yu, M. Zhang, P. Zhang, Q. Li and T. Wang, *Journal of Materials Chemistry A*, 2013, 1, 7247-7254.
31. D. Yuan, P. Ci, F. Tian, J. Shi, S. Xu, P. Xin, L. Wang and P. K. Chu, *Journal of Micro/Nanolithography, MEMS, and MOEMS*, 2009, 8, 033012-033012-033017.
32. S. Furukawa and M. Mehregany, *Sensors and Actuators A: Physical*, 1996, 56, 261-266.
33. P. Villa, F. Trifiro and I. Pasquon, *Reaction Kinetics and Catalysis Letters*, 1974, 1, 341-344.
34. J. E. Herrera and D. E. Resasco, *The Journal of Physical Chemistry B*, 2003, 107, 3738-3746.
35. Z. Xu, Z. Li, X. Tan, C. M. Holt, L. Zhang, B. S. Amirkhiz and D. Mitlin, *RSC Advances*, 2012, 2, 2753-2755.
36. Y. Gogotsi, *ACS nano*, 2014, 8, 5369-5371.
37. D. Cai, B. Liu, D. Wang, L. Wang, Y. Liu, H. Li, Y. Wang, Q. Li and T. Wang, *Journal of Materials Chemistry A*, 2014, 2, 4954-4960.
38. S. Li and X. Wang, *Journal of Power Sources*, 2015, 282, 394-400.
39. E. Frackowiak and F. Beguin, *Carbon*, 2001, 39, 937-950.
40. G. Barral, F. Njanjo-Eyoke and S. Maximovitch, *Electrochimica Acta*, 1995, 40, 2815-2828.
41. G. Brug, A. Van Den Eeden, M. Sluyters-Rehbach and J. Sluyters, *Journal of electroanalytical chemistry and interfacial electrochemistry*, 1984, 176, 275-295.
42. L. Gassa, J. Vilche, M. Ebert, K. Jüttner and W. Lorenz, *Journal of Applied Electrochemistry*, 1990, 20, 677-685.
43. M. E. Orazem and B. Tribollet, *Electrochemical impedance spectroscopy*, John Wiley & Sons, 2011.
44. B. E. Conway, *Electrochemical Supercapacitors: Scientific Fundamentals and Technological Applications*, Springer, 1999.
45. M. Li, S. Xu, C. Cherry, Y. Zhu, R. Huang, R. Qi, P. Yang, L. Wang and P. K. Chu, *Electrochimica Acta*, 2014, 149, 18-27.
46. Y.-M. Wang, X. Zhang, C.-Y. Guo, Y.-Q. Zhao, C.-L. Xu and H.-L. Li, *Journal of Materials Chemistry A*, 2013, 1, 13290-13300.
47. R. B. Rakhi, W. Chen, D. Cha and H. N. Alshareef, *Nano letters*, 2012, 12, 2559-2567.
48. H. Wang, C. M. Holt, Z. Li, X. Tan, B. S. Amirkhiz, Z. Xu, B. C. Olsen, T. Stephenson and D. Mitlin, *Nano Research*, 2012, 5, 605-617.

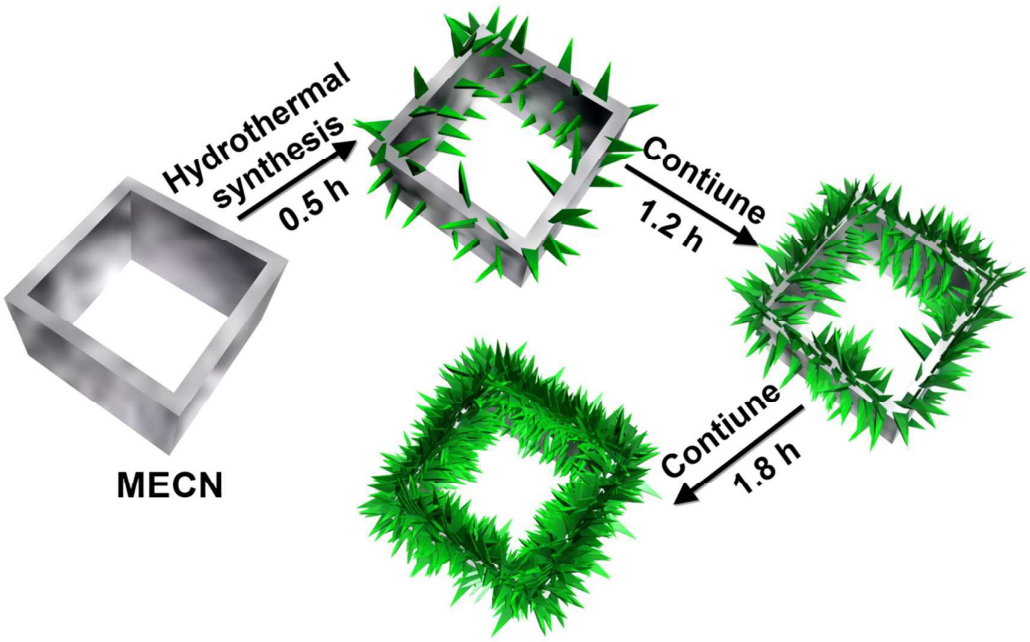

Fig. 1 Schematic illustration of the growth phase of $CoMoO_4$/MECN with different hydrothermal time and formation mechanism of the $CoMoO_4$ nanostructure on the side wall.

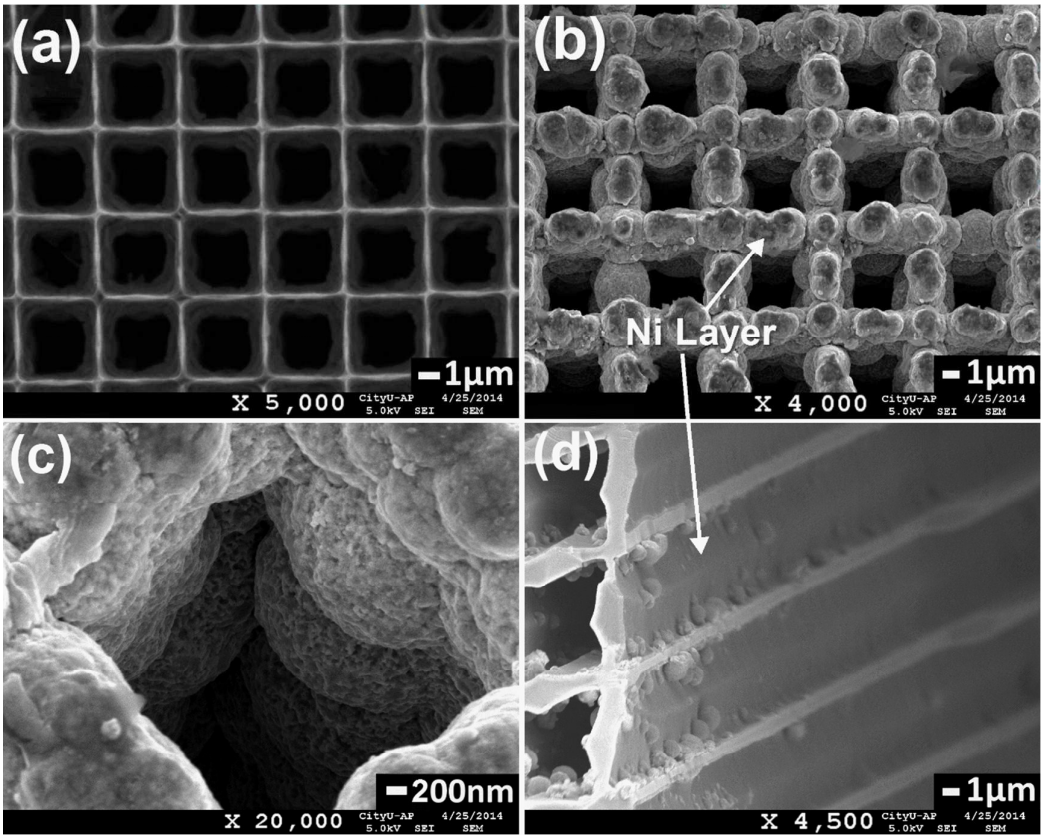

Fig. 2 FE-SEM images acquired from (a) the ordered Si-MCPs; (b) surface of nano-Ni covered MECN; (c) Structure of the porous nano-Ni; (d) Cross-sectional view of the nano-Ni covered MECN.

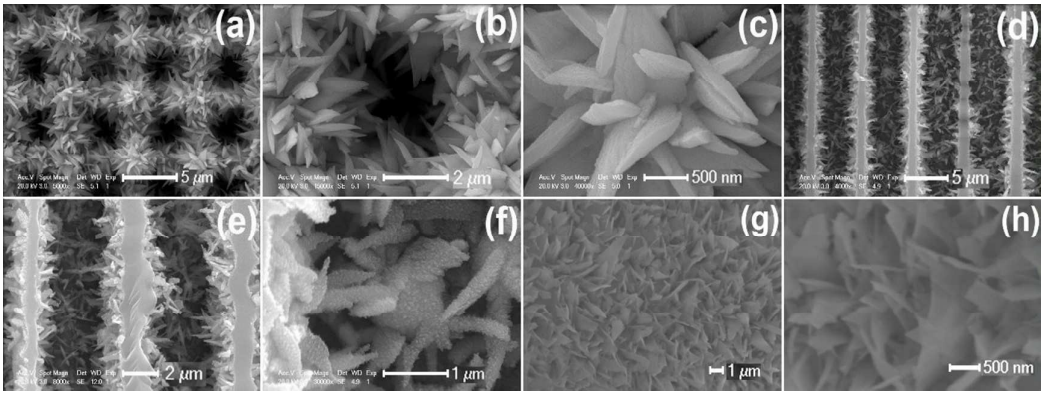

Fig. 3 (a)-(c) Top surface SEM images of the $CoMoO_4$/MECN (1.8h) at different magnifications; (d)-(f) cross-sectional SEM morphology of the $CoMoO_4$/MECN (1.8h) at different magnifications; (g)-(h) surface SEM images of the $CoMoO_4$/Ni/Si (sample-2D, 1.8h) at different magnifications.

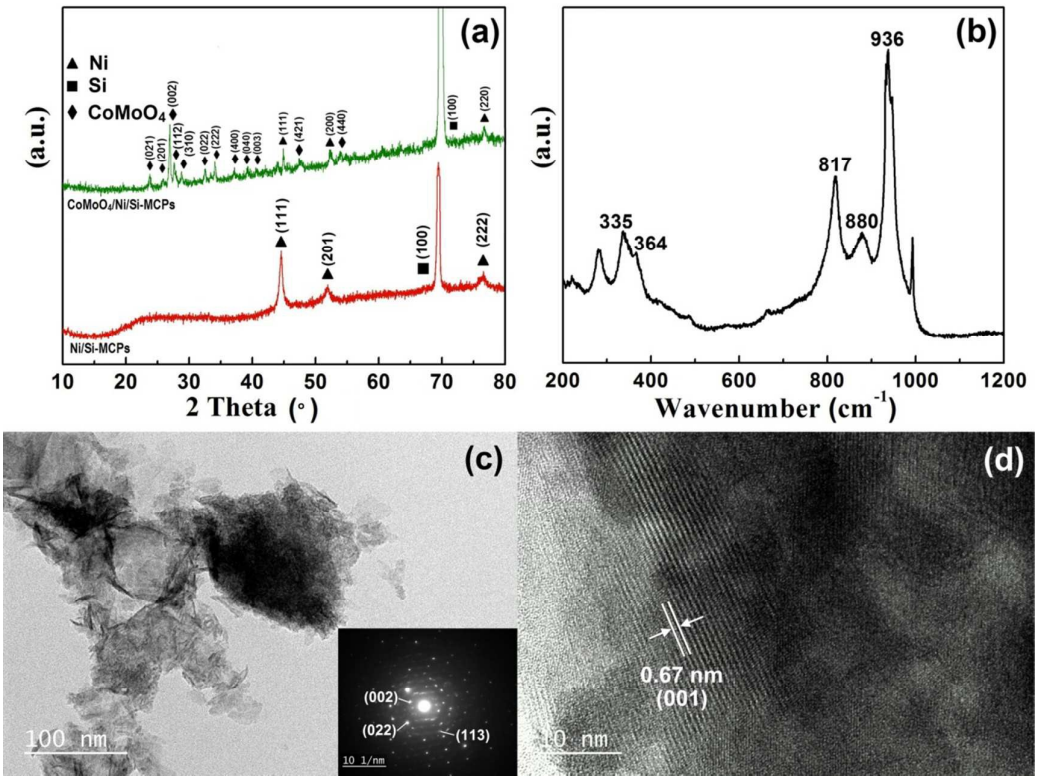

Fig. 4 (a) XRD patterns of $CoMoO_4$/MECN (1.8h) with the black line on the bottom representing the XRD pattern of MECN; (b) The Raman spectra of $CoMoO_4$/MECN; (c) shows a SAED pattern of an individual nanoflack; (d) HR-TEM image of the $CoMoO_4$ crystal lattices.

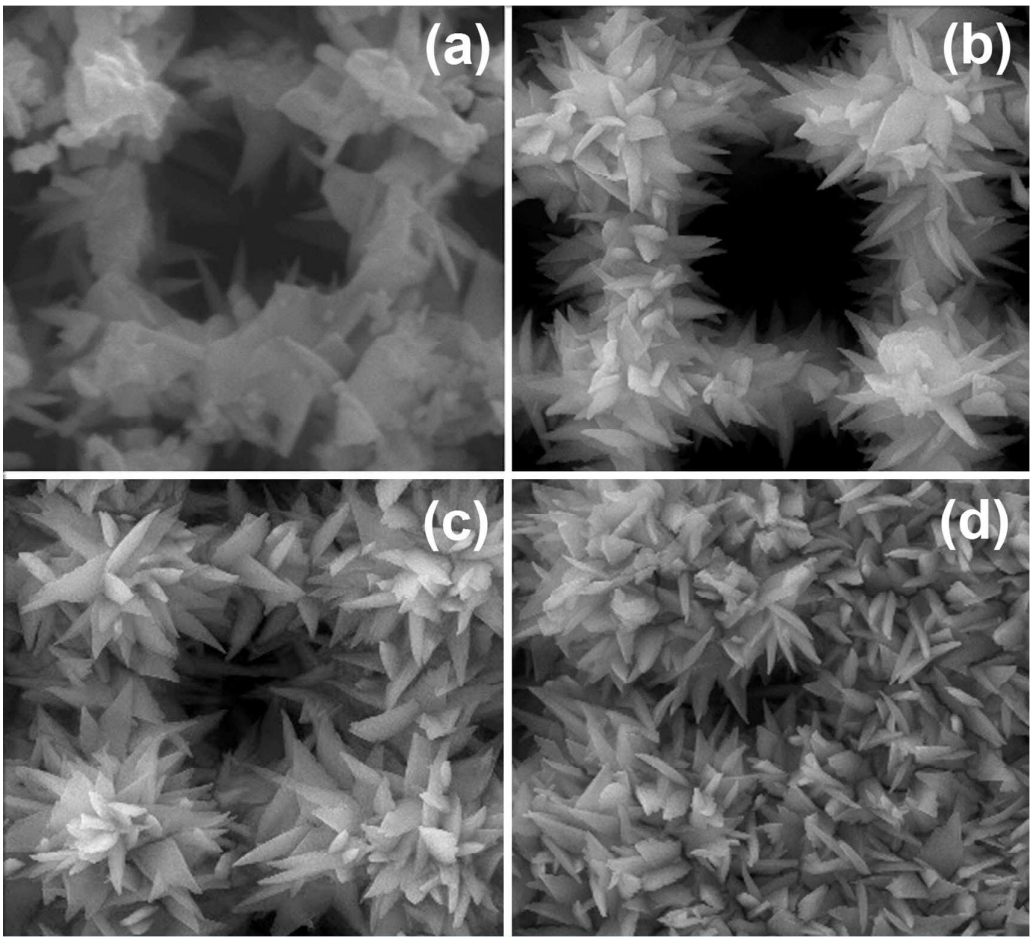

Fig. 5 FE-SEM images of nanostructured $CoMoO_4$ flakes on the micro-channel of the MECN with different hydrothermal time: (a) 0.5 hour; (b) 1.2 hour; (c) 1.8 hour; (d) 2.5 hour.

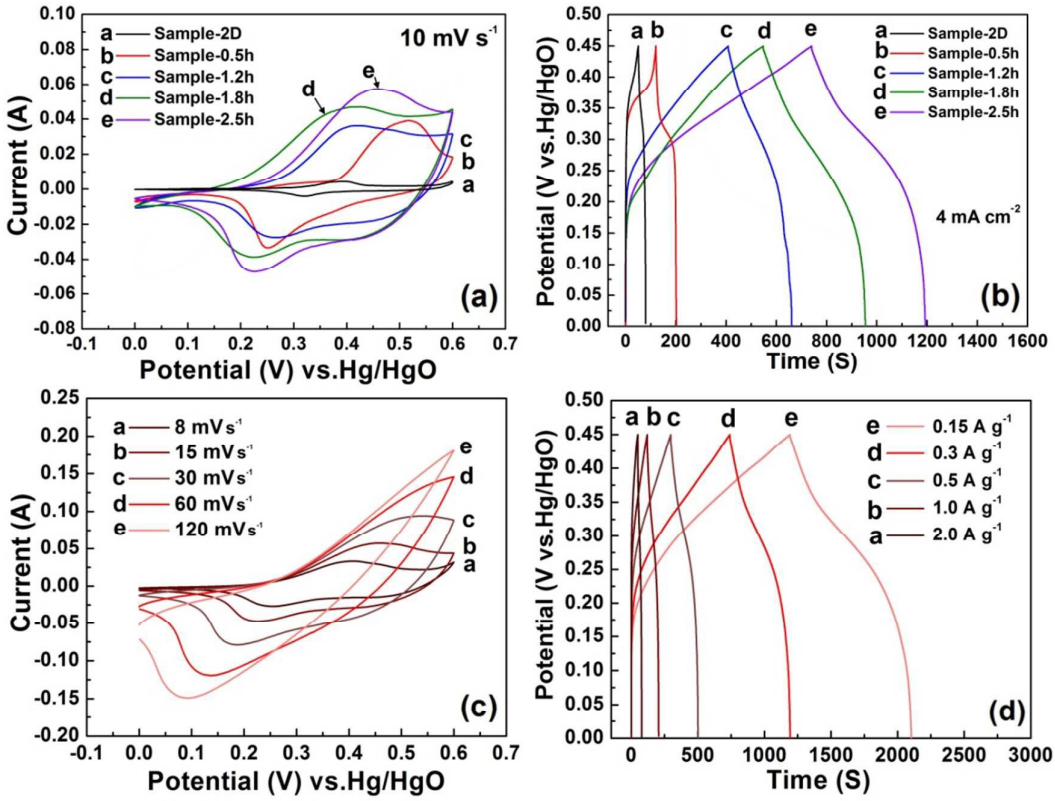

Fig. 6 (a) Cyclic voltammetry curves of the $CoMoO_4$/Ni/Si (2D) electrode and $CoMoO_4$/MECN with different reaction time of 0.5, 1.2, 1.8 and 2.5 hours at scanning rates of 10 mV s^{-1}; (b) 4 mA cm^{-2} charge/discharge curves of newly fabricated $CoMoO_4$/MECN electrode for different reaction time of 0.5, 1.2, 1.8 and 2.5 hours; (c) CV curves of $CoMoO_4$/MECN (2.5h); (d) First discharge curves of $CoMoO_4$/MECN (2.5h).

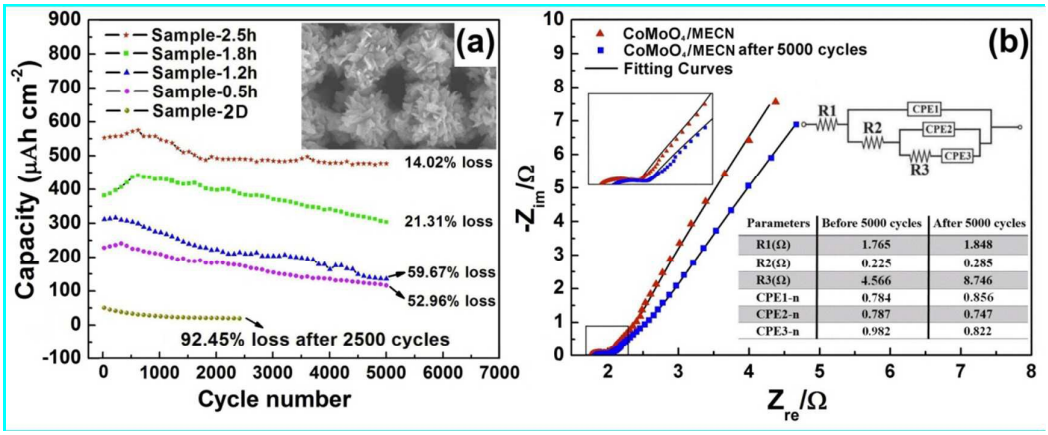

Fig. 7 (a) Long-term performance of the $CoMoO_4$/MECN assessed at a charging-discharging current density of 20 mA cm^{-2}; (b) Nyquist plots of the $CoMoO_4$/MECN electrodes in a 2 M KOH solution before and after 5,000 cycles in the long-term performance test with the equivalent circuit and element values fitting the impedance curve.

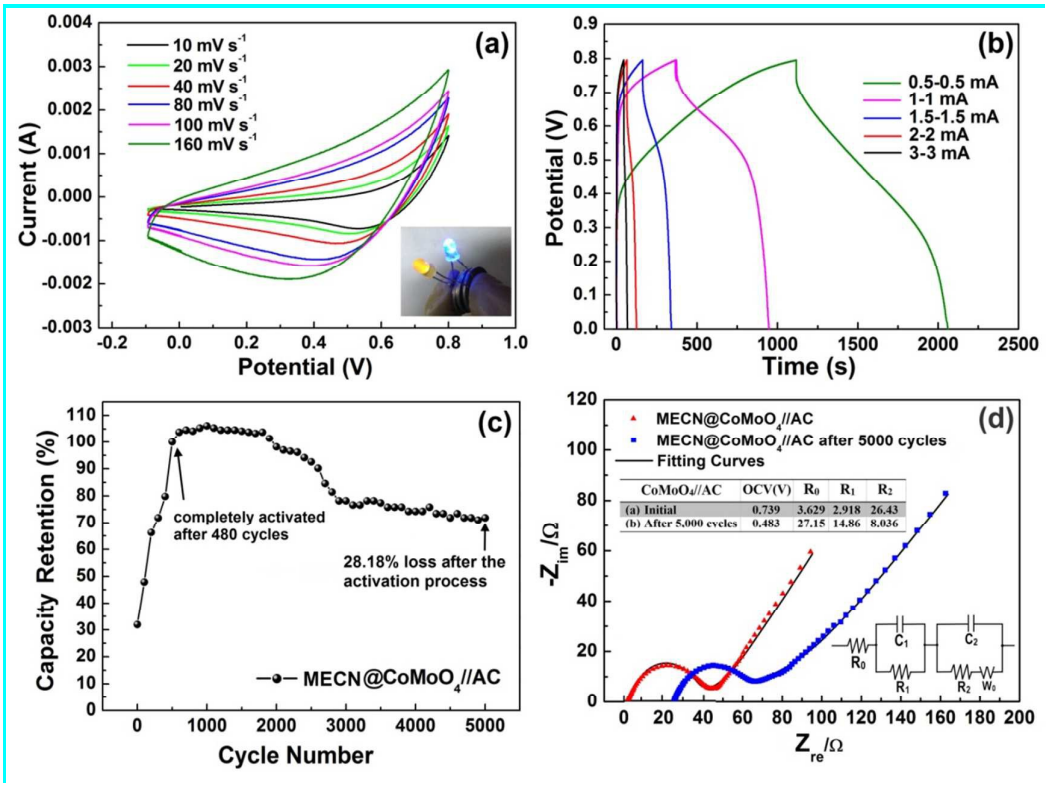

Fig. 8 (a) CVs acquired at different scanning rates between 0 and 0.8V of the $CoMoO_4$ hybrid device; (b) Charge-discharge curves at different current densities of the hybrid device; (c) Cycling stability of the 5000 cycles of device at large current density; (d) Nyquist plots of the MECN@ $CoMoO_4$//AC before and after 5,000 cycles in the long-term performance test with the equivalent circuit and element values fitting the impedance curve.

Graphical Abstract:

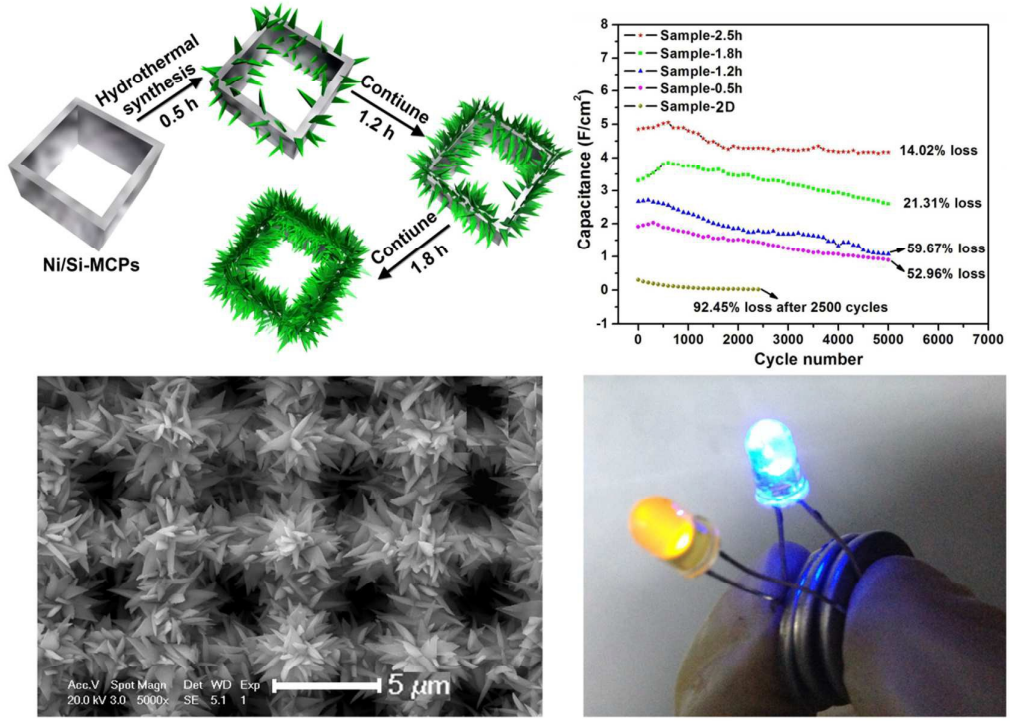

The paper studied the formation mechanism and growth process of nanostructured ordered $CoMoO_4$ fabricated on Macroporous Electrically conductive Network (MECN). The relationship among the reaction time, morphology, formation mechanism of the $CoMoO_4$ nanostructure, and faradaic behavior is studied. After an optimal hydrothermal synthesis time of 2.5 h, the $CoMoO_4$ faradaic electrode has a capacitance of 32.40 mAh g^{-1} (492.48 μAh cm^{-2}) at constant current density of 1 A g^{-1} and retention ratio of 85.98% after 5,000 cycles. By using the $CoMoO_4$/MECN electrode as the positive electrode and CNTs/nickel foam (CNTs/NF) as the negative electrode, the electrods were packaged with CR2025 batteries case. The packaged $CoMoO_4$ hybrid device exhibits stable power characteristic (5,000 times with 71.82% retention) and after charging each hybrid device for 10 s, three devices in series can power two 5 mm diameter light-emitting diodes (LED) efficiently.